Cell Reports
Physical Science

CellPress
OPEN ACCESS

Article

Nanoscale state-of-charge heterogeneities within polycrystalline nickel-rich layered oxide cathode materials

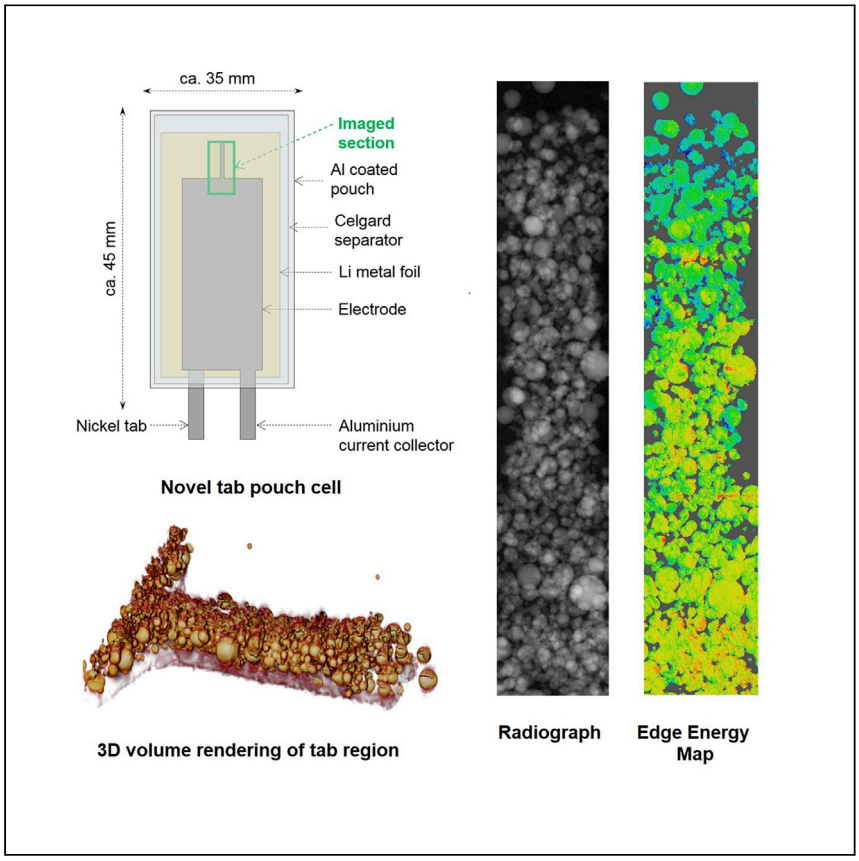

Chun Tan, Andrew S. Leach, Thomas M.M. Heenan, ..., Johanna Nelson Weker, Daniel J.L. Brett, Paul R. Shearing

p.shearing@ucl.ac.uk

Highlights

In situ pouch cell design that is adaptable to various characterization methods

Combined lab-based micro-CT and synchrotron XANES imaging approach

Insights into spatio-temporal dependence of degradation in NMC811

There is significant interest in the energy storage community for *in situ* studies because of the codependence of spatial and temporal effects on the performance of an electrochemical cell. Tan et al. report a tab pouch cell design that maintains fidelity to commercially relevant cells while still allowing 3D measurements at the nanoscale.

Tan et al., Cell Reports Physical Science *2*, 100647
December 22, 2021 © 2021
https://doi.org/10.1016/j.xcrp.2021.100647

Cell Reports
Physical Science

CellPress
OPEN ACCESS

Article

Nanoscale state-of-charge heterogeneities within polycrystalline nickel-rich layered oxide cathode materials

Chun Tan,[1,2] Andrew S. Leach,[1,2] Thomas M.M. Heenan,[1,2] Huw Parks,[1,2] Rhodri Jervis,[1,2] Johanna Nelson Weker,[3] Daniel J.L. Brett,[1,2] and Paul R. Shearing[1,2,4,*]

SUMMARY

Nickel-rich cathodes ($LiNi_xMn_yCo_{1-x-y}O_2$, x > 0.6) permit higher energy in lithium-ion rechargeable batteries but suffer from accelerated degradation at potentials above 4.1 V versus Li/Li^+. Here, we present a proof-of-concept *in situ* pouch cell and methodology for correlative 2D synchrotron transmission X-ray microscopy with 3D lab-based micro-CT. XANES analysis of the TXM data enables tracking of Ni edge energy within and between the polycrystalline NMC811 particles embedded in the operating electrode through its initial delithiation. By using edge energy as a proxy, state-of-charge heterogeneities can be tracked at the nanoscale, revealing the role of cracked particles as potential nucleation points for failure and highlighting the challenges in achieving uniform (de-)lithiation. We propose, in future work, to leverage the pouch cell design presented here for longitudinal TXM-XANES studies of nickel-rich cathodes across multiple cycles and operating variables and investigate the effect of dopants and microstructural optimization in mitigating degradation.

INTRODUCTION

Nickel-rich transition metal oxide materials ($LiNi_xMn_yCo_{1-x-y}O_2$, x > 0.6) are of great interest for achieving immediate improvements in the energy density of Li-ion batteries and for risk reduction within the Li-ion battery supply chain arising from the geopolitical risk of Co mining. Increasing the Ni content within these materials has the effect of increasing their reversible specific capacity; for instance, NMC811 ($LiNi_{0.8}Mn_{0.1}Co_{0.1}O_2$) has a reversible specific capacity of ~200–220 mAh g^{-1}, compared to NMC111 ($LiNi_{0.33}Mn_{0.33}Co_{0.33}O_2$), with a lower reversible specific capacity of 145 mAh g^{-1}.[1]

An increase in Ni content in NMC materials leads to accelerated degradation through various mechanisms, summarized by Li et al.[1] to be a combination of parasitic reactions occurring with the electrolyte, cation mixing within the layered oxide structure, transition metal dissolution, and oxygen release. This potentially complicates their adoption in applications requiring extended cycle life such as in electric vehicles (EVs), because manufacturers' warranties on battery packs are typically on the order of ~8 years or 100,000 miles.[2]

Recent developments in X-ray characterization tools have provided unprecedented insight into the structural, chemical, and electronic states of materials, and these tools have been harnessed to probe Li-ion batteries both in the lab and in large-scale

[1]Electrochemical Innovation Lab, Department of Chemical Engineering, University College London, Torrington Place, London WC1E 7JE, UK

[2]The Faraday Institution, Quad One, Harwell Science and Innovation Campus, Didcot OX11 0RA, UK

[3]Stanford Synchrotron Radiation Lightsource, SLAC National Accelerator Laboratory, 2575 Sand Hill Road, Menlo Park, CA 94025, USA

[4]Lead contact

*Correspondence: p.shearing@ucl.ac.uk

https://doi.org/10.1016/j.xcrp.2021.100647

synchrotron facilities.[3] One particular technique of interest is full-field transmission X-ray microscopy (TXM) and tomography, offering a spatial resolution down to ~30 nm that can be used to examine the microstructure of battery electrodes with an intricate level of detail, revealing subparticle defects such as inhomogeneities and cracking.[4] At synchrotron facilities, spectroscopic TXM can be achieved around the hard X-ray region (~5–12 keV), which is highly desirable because the K-edge of transition metals (e.g., Co, Ni, Mn, Fe) common in Li-ion$^+$ electrode materials lie within that region.[5,6] Dual-energy imaging above and below an element-specific absorption edge permits the identification of an element of interest, while by imaging at multiple energies around the absorption edge, nanoscale oxidation state maps can be reconstructed through X-ray absorption near-edge structure (XANES) analysis.[5–8]

While XANES studies are commonly performed on bulk materials, the advantages of obtaining spatially resolved information at the nanoscale have been demonstrated by various authors,[3,5,6,9–12] particularly given the broader role that heterogeneities play in the nucleation of battery degradation. A number of *ex situ* spectroscopic TXM studies have been performed on NMC-based materials, including Ni-rich NMC materials. Yang et al.[9] tracked the elemental concentrations of Ni, Mn, and Co within Li-Mn-rich NMC recovered from cells taken to different cycle numbers (up to 200 cycles). Tian et al.[10] detected significant state-of-charge heterogeneities in polycrystalline NMC622 after both chemical and electrochemical delithiation, cautioning that surface chemistry effects were not replicated in chemically delithiated samples. More recently, Xu et al.[12] examined the influence of particle morphology on charge distribution within particles, comparing between polycrystalline rod- and grain-shaped NMC811 through a combination of *ex situ* spectroscopic TXM and 3D TXM.

Due to constraints in sample size, acquisition time, and radiation dose, most nanoscale two-dimensional (2D) and 3D investigations into battery materials are performed on *ex situ* samples; a common preparation technique involves the extraction of active material particles into thin capillary tubes of ~100 μm in diameter. *In situ* and *operando* studies can offer a wealth of information unavailable to post-mortem characterization by allowing the same region of interest to be directly compared at various states of charge. These studies can also be extended longitudinally to investigate the effects of cycling and aging on the active particles through the acquisition of samples prepared at various conditions or through an *in situ* electrochemical cell setup. Wang et al. first demonstrated *in situ* chemical mapping through XANES TXM of a CuO anode undergoing lithiation,[13] followed later by an *operando* study on a $LiFePO_4^+$ electrode, monitoring the phase change from $LiFePO_4$ to $FePO_4$ during delithiation within an *operando* Kapton-windowed coin cell.[14] However, it is known that Kapton film has a high water vapor transmission rate, precluding long duration investigations, as moisture ingress is detrimental to the organic electrolyte within Li-ion cells.[15] More recently, Alvarado et al.[16] explored the effects of thermal stress on the chemical composition of NMC811 particles through *in situ* X-ray spectromicroscopy while heating chemically delithiated samples to elevated temperatures.

We have previously proposed a sample preparation strategy that produces samples suitable for lab-based X-ray nano-computed tomography (nano-CT) smaller than 100 μm in size and with a turnaround time of <1 min per sample.[17] In addition to rapid sample preparation, the advantages of this laser-milling technique include the ability to perform vertical stitching of multiple tomograms, mosaic acquisition (which allows the acquisition of samples of larger diameters at high resolution), and highly localized laser-induced sample damage due to the low overall dose and minimal sample heating. This allows

the sample to be cycled electrochemically, and for this purpose, we designed a specialized pouch cell suited to *in situ* and *operando* X-ray characterization across multiple length scales down to the nanoscale.

Here, we present a proof-of-concept correlative *in situ* 3D micro-CT and 2D spectroscopic TXM study on a polycrystalline NMC811 electrode in a half-cell arrangement within our specialized tab pouch cell during its initial delithiation (charge). For the first time to the authors' knowledge, the same particles within a battery electrode measured at their pristine and delithiated states with spectroscopic TXM were correlated with overall 3D microstructure, revealing the direct effect that manufacturing defects within particles have on the state-of-charge distribution within the particles after the initial delithiation. We believe that our proposed approach would minimize radiation-induced sample damage and greatly increase throughput during highly limited synchrotron beam-time by leveraging the wider availability of lab-based instrumentation for more time-consuming 3D acquisition.

RESULTS

Novel *in situ* tab pouch cell

We have previously demonstrated a rapid tab milling technique for nano-CT sample preparation on *ex situ* Li-ion battery electrode samples,[17] and the technique has been adapted to mill electrodes of dimensions suitable for construction into fully operating pouch cells in a half-cell arrangement, with Li-metal as the counter electrode. These pouch cells are ideal for X-ray characterization experiments in transmission or reflection modes using either lab-based or synchrotron sources.

The gold standard to measure subparticle chemical information in real time, 3D *operando* XANES-CT, remains out of reach, however. This is because acquisition times are more than an order of magnitude longer than desired from a temporal resolution, energy resolution, and radiation damage standpoint.[5] It is possible to couple faster 2D spectroscopic TXM with a 3D micro-CT dataset of the same volume acquired before or after TXM measurements to gain microstructural information of the electrode. With a multimodal correlative approach, first proposed by Yang et al.,[9] it is possible to obtain the approximate edge energies of clusters of particles within the electrode, and thus detect changes in the chemical state of elements of interest within the particles.

As shown in Figure 1, the specialized pouch cell has overall dimensions of ~35 × 45 mm with Ni (negative) and Al (positive) tabs protruding from one end. Within the cell, the Ni tab is in contact with Li-metal foil cut to be slightly larger than the positive electrode. This is kept electrically insulated from the positive electrode with a standard Celgard 2325 separator. The positive electrode is a standard NMC811 electrode cut into 3 connected rectangular sections, as described in the Experimental procedures section. To maintain adequate transmission and signal-to-noise ratio, it is imperative that the dimensions of the object being imaged is within the field of view of the detector. In this arrangement, the region of interest fits fully within the field of view of the detector, while the other elements of the pouch cell within the field of view are relatively featureless and do not significantly attenuate the beam across a wide angular range, thus allowing a relatively high-quality tomographic reconstruction to be achieved, as shown in Figure 2.

Despite the presence of shading artifacts introduced by the high aspect ratio sample, the contrast-to-noise ratio is sufficient for individual NMC811 particles within

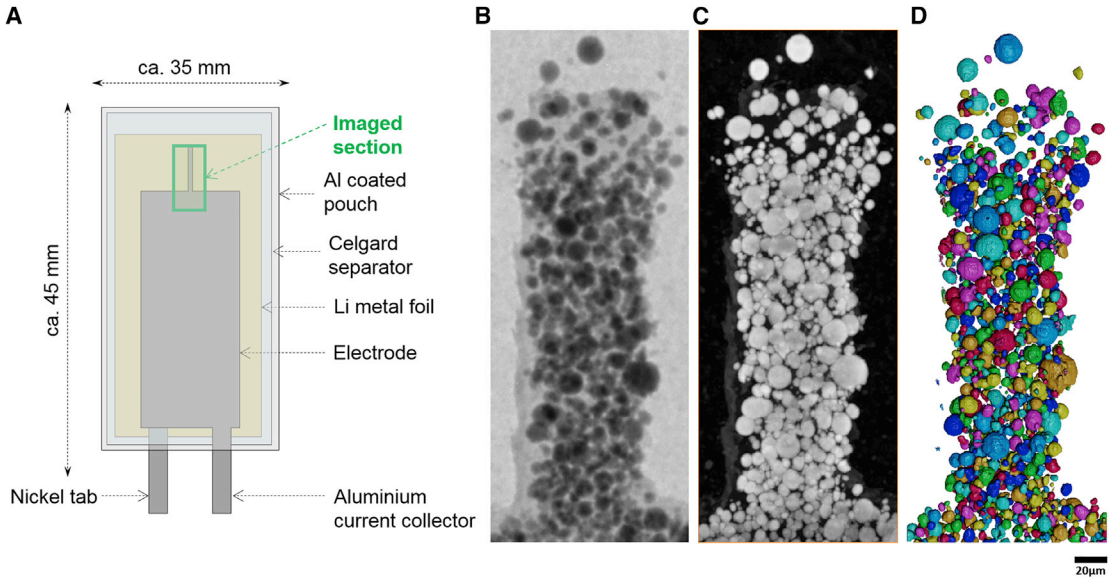

Figure 1. Novel *in situ* tab pouch cell

(A) Schematic of the specialized pouch cell used for spectroscopic TXM and micro-CT.

(B) Radiograph of the tab section used for imaging at the 0° angle, acquired using the ZEISS Xradia Versa 520 micro-CT instrument.

(C) Image stack projection of the reconstructed volume.

(D) A volume rendering of individually labeled particles segmented from the reconstructed volume.

the cell to be segmented, and these individually labeled particles are shown overlaid in Figure 2B.

Long-duration exposure to the synchrotron beam for the acquisition of many energy points caused significant radiation-induced degradative changes to the carbon and binder domain, which will inform our future data acquisition strategy. This can be observed at the tip of the tab—the regions of Figures 2A and 2C outlined in yellow, where dose-dependent swelling of the carbon binder domain becomes apparent in the micro-CT volume taken, after the region was exposed to the synchrotron X-ray beam over the course of ~12 h. This is to be expected, because absorption by the sample increases significantly as the incident beam approaches the absorption edge, leading to more secondary radiation and consequently a higher radiation dose.[18,19]

The above highlights the advantages of a combined 3D lab-based and 2D synchrotron-based data collection strategy: dose minimization for (longer) 3D scans may be accomplished through the use of low-flux lab-based sources, while still benefitting from the richness of the data acquired from a synchrotron source.

Electrochemical data and bulk XANES spectra of tab pouch cell

The voltage-capacity profile of the specialized pouch cell, delithiated to 4.3 V versus Li/Li^+ at the beamline between imaging steps (marked with the gray and red circles), is presented in Figure 3A, along with the bulk normalized absorbance calculated from the merged mosaic images in Figure 3B. A cell with the same cathode material was also measured at the B18 beamline at Diamond Light Source before the TXM experiment, and the XANES spectra of that cell at its pristine and delithiated state is presented in Figure 3C. It is hypothesized that the difference between the bulk normalized absorbance from the mosaics acquired in the TXM experiment and the

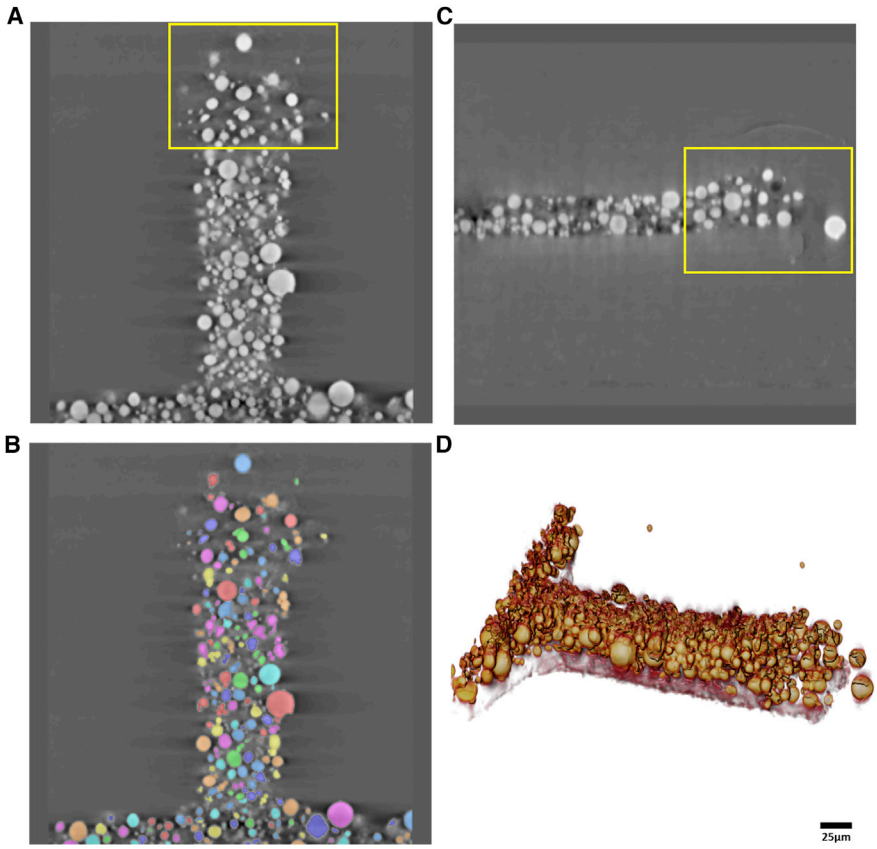

Figure 2. Micro-CT of tab section within novel pouch cell

(A–C) Ortho-slices of the micro-CT volume of the specialized pouch cell at various perspectives.
(D) Volume rendering of the same volume, with the current collector shown at the bottom.

XANES spectra of the same material acquired at the B18 beamline, shown in Figure 3D, arises from a few factors: a positive zero error introduced from differences in the calibration of the monochromators, peak broadening due to the larger energy steps used in the TXM experiment, and a difference in normalization due to the limited energy points used in the TXM experiment.

The beam energies used for the multi-energy nano-imaging experiment were selected with *a priori* knowledge of the bulk XANES profile of a similar sample at its pristine and delithiated state, which would theoretically permit the acquisition of significantly fewer energy points compared to bulk XANES, in which the number of energy points acquired is typically on the order of 10^3. A total of 7 energy points were collected due to time constraints: the radiographs collected at 8,300 and 8,320 eV served as the pre-edge points, while those acquired at 8,800 and 8,950 eV served as the post-edge points for normalization. Three energy points were acquired around the Ni edge, at 8,347, 8,353.5, and 8,360 eV.

While it was originally anticipated from the XANES spectra that the base of the peak of the Ni K-edge, where the normalized absorbance is close to 0, is ~8,347.5 eV (which resulted in the selection of this energy as the first point after the pre-edge points), the positive zero error in beam energy would in effect mean that the TXM mosaic images were acquired at an energy slightly higher than 8,347.5 eV. Since the slope of the edge is relatively steep, the normalized absorbance of this point

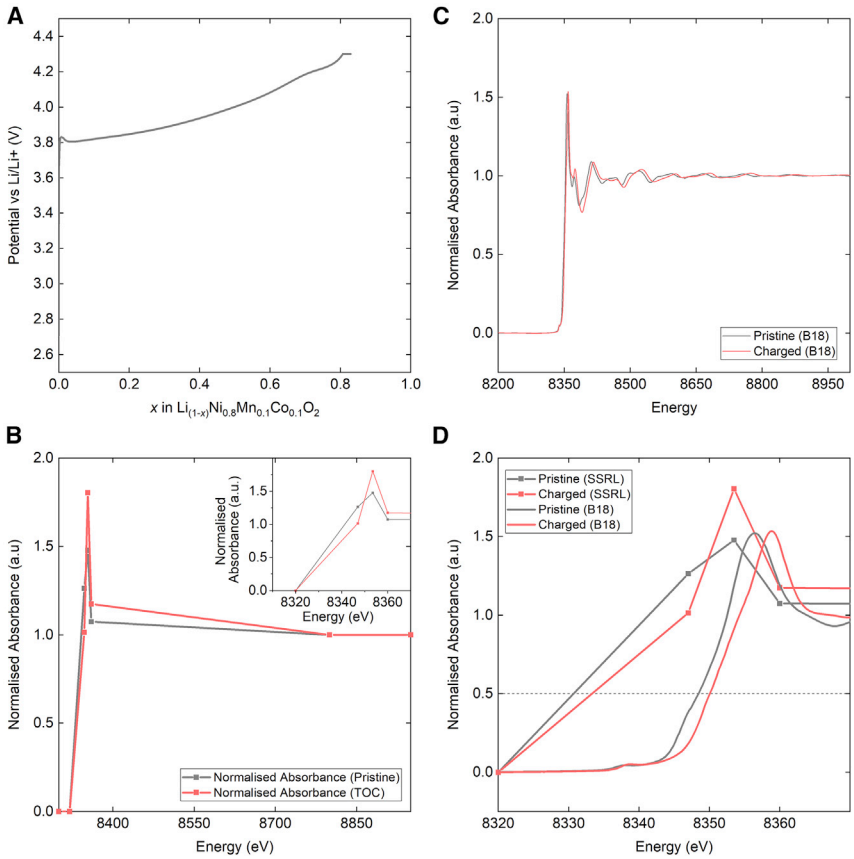

Figure 3. Electrochemical data and bulk XANES spectra

(A) Specific capacity-voltage curve of the initial charge step of the specialized pouch cell delithiated from its pristine state (delithiated from ~3 to 4.3 V versus Li/Li^+), assuming no electrons were used in side reactions.

(B) Normalized bulk absorbance of the mosaics acquired at both the pristine (gray points and line) and the delithiated (red points and line) states around the Ni edge.

(C) XANES spectra of the same material in a specialized pouch cell acquired at the B18 beamline at Diamond Light Source at both the pristine (black line) and the delithiated (red line) states.

(D) The same spectra in (B) and (C) between 8,320 and 8,370 eV with the horizontal dotted line representing half the edge jump intensity, where the edge energy is linearly interpolated.

is correspondingly higher in the TXM data. This is compounded by the small number of energy points acquired because the edge energy, defined as the energy at half the edge-jump intensity,[20] is linearly interpolated from the line between the 8,320 and 8,347.5 eV acquisition point.

Thus, because of the systematic bias introduced by the factors above, the edge energy calculated from the TXM data is not presented here in absolute terms. Instead, the relative changes in edge energy between the pristine and delithiated datasets is considered in the following sections, with 0 defined as 8,330 eV.

Edge energy maps of electrochemically active tab section

A correlation between Ni edge energy and the oxidation state of the Ni ion, analogous to the measurements O'Grady et al.[21] performed on Ni-metal hydride batteries, is observed from bulk XANES measurements shown in Figure 3D when comparing between the lithiated and delithiated states. Therefore, as described

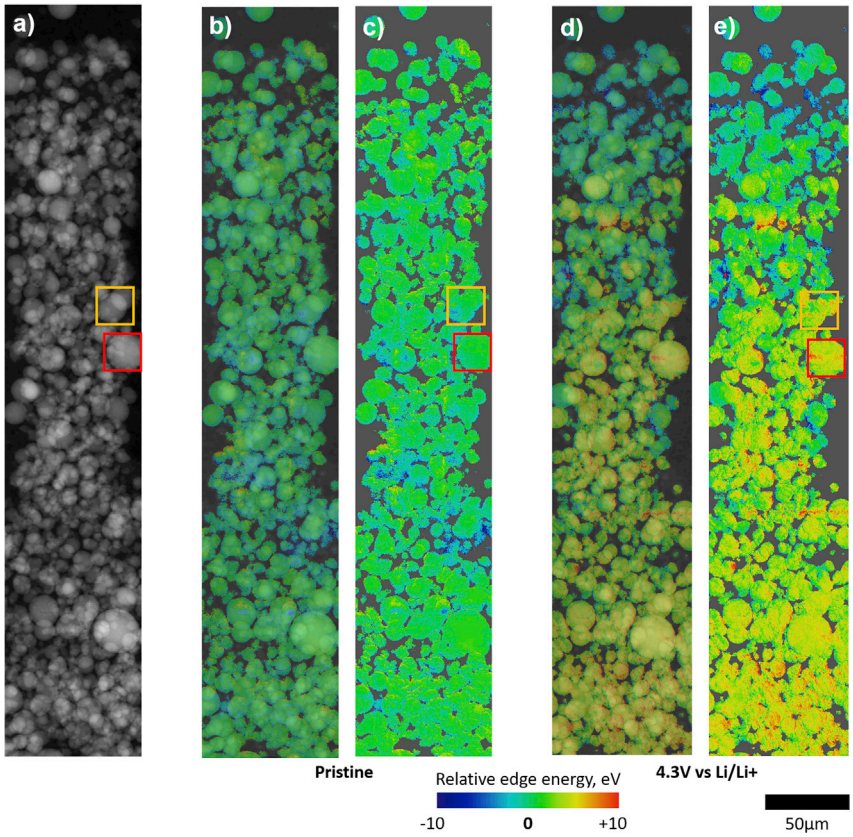

Figure 4. Relative edge energy maps around the Ni edge

(A–D) (A) Stitched reference-corrected mosaic of the imaging tab section of the pouch cell acquired at 8,950 eV at the pristine state. Relative edge energy maps at the (B and C) pristine and (D and E) delithiated states, with (B and D) showing the edge energy maps overlaid on the stitched reference-corrected mosaic; 0 was defined as 8,330 eV. Both pristine and delithiated mosaics were acquired at 7 energy points: 8,300, 8,320, 8,347, 8,353.5, 8,360, 8,800, and 8,950 eV. Examples of particles with defects visible in 2D are shown in the red, orange, and yellow boxes.

by Xu et al.,[12] the Ni edge energy can be used as a proxy to measure state-of-charge within an NMC electrode. A comparison of the relative edge energy maps of the electrode at the pristine (Figure 4C) and delithiated (Figure 4E) states reveals significant state-of-charge heterogeneity within particles of all diameters within the electrode once the cell is delithiated, as opposed to a relatively homogeneous distribution in the pristine sample. This is despite there being no voltage hold or current passed across the cell during imaging; the mosaic images were acquired with the cell left at open circuit. The same region of interest was measured on the delithiated cell after ~2 h of relaxation (during which time another sample was imaged in the beam), and thus, charge balancing that occurs across a longer time frame may not be captured here, although this is not expected to be significant, as discussed by Tian et al.[10]

Some particles in the pristine state exhibiting manufacturing defects, such as internal voids, cracks, and calendaring-induced pulverization, can be identified in 2D. Two examples of these defects are highlighted in red (lower density) and orange (cracks) boxes in Figures 4 and 5. The initial goal of micro-CT imaging was to obtain spatial information about the positioning of the particles within the electrode layer (illustrated by the volume rendering in Figures 5B and 5D), and thus

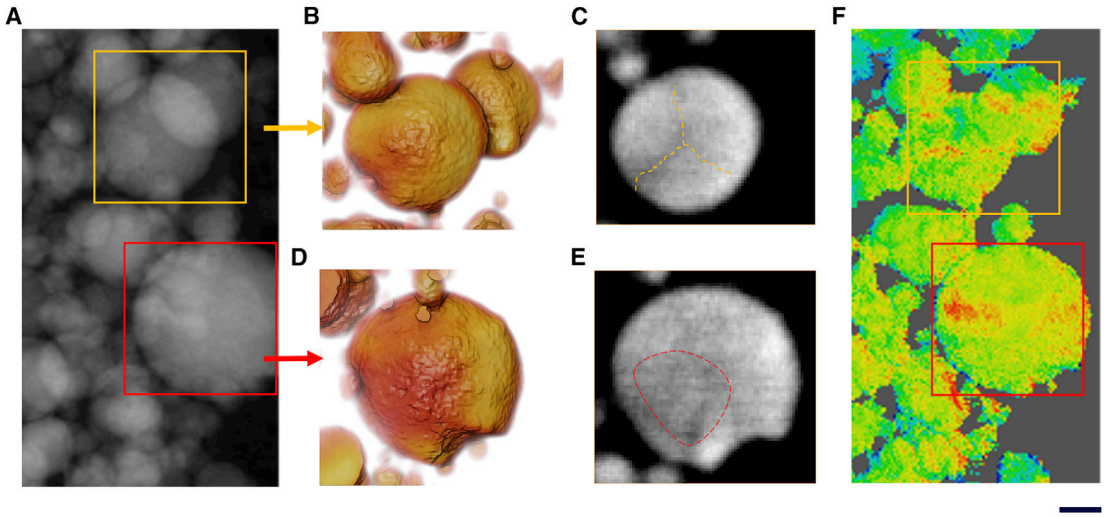

Figure 5. Region of interest analysis

(A) Magnified region of interest containing examples of defective particles cropped from the stitched reference-corrected mosaic of the imaging tab section acquired with TXM at 8,950 eV at the pristine state.

(B and C) From the 3D micro-CT volume of the same cell: (B) a volume rendering of the region of interest indicated by the orange box and (C) a virtual slice of the defective particle showing cracks highlighted by the orange dotted line.

(D and E) A volume rendering of the region of interest indicated by the red box (D), and (E) a virtual slice of the defective particle showing a lower-density region within the red dotted circle.

(F) Magnified relative edge energy map obtained in the delithiated state of the same region of interest, acquired with TXM.

Scale bar is 5 μm for all of the images in the figure.

a relatively large pixel size was selected. However, as shown in Figures 5C and 5E, it is possible to visualize some defects just smaller than the spatial resolution of the reconstructed data, which would result in these voxels having a smaller electron density than the bulk particle and thus appearing less bright. Thus, cross-correlation of the micro-CT data with the 2D mosaic image suggests that when the electrode is delithiated by charging to 4.3 V versus Li/Li^+, the local states-of-charge adjacent to the defect zones are higher than the surrounding regions. We hypothesize that these defect zones could be potential points of failure within the battery, contributing not only to electrolyte degradation but also to irreversible oxygen release arising from over-delithiation. In future work, we aim to measure the same defective particles across numerous cycles to track their contribution to the overall degradation within the cell, and to perform micro-CT imaging at a higher magnification to more clearly identify defects within the particles for correlation with the edge energy maps.

It is evident from Figure 4 that the region close to the top of the imaging tab, which was exposed to significantly more radiation dose during initial setup (on the order of ~12 hs of cumulative beam exposure), does not exhibit any significant edge energy shift between the pristine and delithiated Ni edge energy maps. This is highly indicative that the region has become electrochemically inactive. Some swelling of this region is also observed in the micro-CT volume as described earlier, confirming previous reports of the effect of radiation-induced degradation on the carbon and binder domain, resulting in the electrical disconnection of the particles within the exposed region.

Therefore, the most optimal acquisition strategy in future work that can capture both transient phenomena and longitudinal degradation would logically be a

combination of *in situ* or *operando* studies on dilute electrodes (~1 particle thick), followed by post-mortem studies on thicker electrodes taken to various conditions.

Particle-based Ni edge energy analysis

To examine the influence of the 3D structure of the electrode on the 2D measurement of state-of-charge distribution within the NMC811 electrode, a few particle clusters were extracted from the relative energy maps at the pristine and delithiated state, and these are presented in Figure 6. As the electrode was thicker than a single layer of particles, stacking of particles is observed orthogonal to the current collector (i.e., in the direction of the beam), and therefore a particular region captured within the edge energy maps may consist of multiple superimposed particles. In the case of overlapping particles, it is expected that the edge energy of any pixel of the map (which is obtained from the normalized absorption images acquired at the various energies) would be averaged across all of the particles lying in the same beam path.

Interestingly, variations were observed within the edge energy histograms of the 4 particle clusters as shown in Figure 6F, with 2 distinct peaks ~−0.5 $eV_{relative}$ for clusters c and d compared to ~1 $eV_{relative}$ for clusters b and e. This bifurcation of edge energy histograms ceases to exist in the delithiated state, suggesting variations in Li content within the pristine electrode. While making these comparisons, one should note the energy resolution of the instrumentation, $\Delta E/E$, is on the order of 10^{-4}—hence, the error propagated to the edge energy calculated through linear interpolation between 2 energy points would be far smaller than the difference shown here of 1.5 eV. Furthermore, only relative changes were considered, and the same linear interpolation was carried out on the pristine and charged datasets.

A broadening of the histograms can be observed upon transitioning to the delithiated state, suggesting a wider variation in the local state-of-charge distribution within the particles, which is consistent with the visual observation on the larger mosaics shown in Figures 4E and 4G.

In general, an examination of the four particle clusters above in Figure 6, along with the manufacturing defects shown in Figure 4, reveals the need to examine a large number of particles because of the random nature of heterogeneities and variations in defect population between different battery electrodes. This demonstrates the advantages of the *in situ* technique presented here, namely the acquisition of a sufficiently large population of particles, and the ability to track the same population of particles across time. While single-particle studies may show interesting features, they may not be representative of the bulk electrode.

The superposition of the 2D relative edge energy map with a post-mortem 3D micro-CT volume taken of the same region of interest not only provides additional spatial information about the position of particles within the 2D map to decouple the contribution to edge energy from stacked particles in the same line of sight but also demonstrates the viability of identifying internal defects within particles. These defects can be cross-correlated with inhomogeneities in the oxidation state detected in the edge energy map, providing direct evidence of defect-induced state-of-charge heterogeneity within single particles in the electrode matrix. As previously discussed, these state-of-charge heterogeneities do not resolve upon cell relaxation and may act as a source of continued electrolyte degradation when cells are stored at a high state-of-charge, as well as nucleation points for oxygen release and rock salt formation within the crystal structure during prolonged cycling.

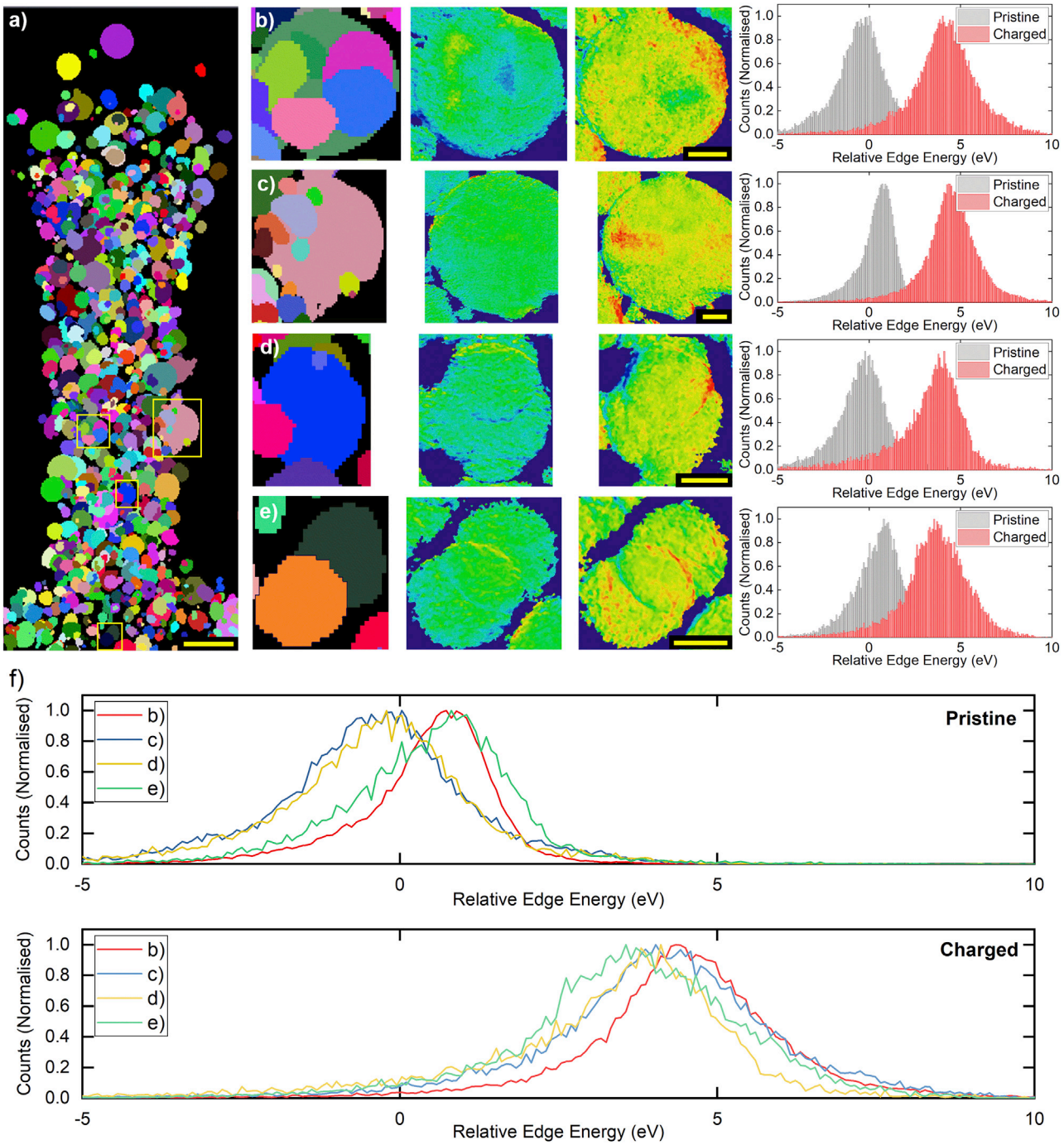

Figure 6. Particle-based edge energy analysis

(A) Intensity maxima projection of the numbered label field of the micro-CT volume, where each particle is assigned a unique integer.

(B–E) From left to right: cropped intensity maxima projection around the selected particles from the micro-CT data; 2D edge energy map of the same region at the pristine and delithiated states; and corresponding histograms of the cropped maps, all from the TXM data. (B) Particle #438 in elf green, (C) particle #397 in salmon pink, (D) particle #516 in blue, and (E) particle #788 in orange.

(F) Histogram line profiles of all of the particle clusters shown in (B–E) at the pristine and delithiated states.

Scale bar for (A) is 25 μm and all of the other scale bars are 4 μm.

The heterogeneities resolved through this combined TXM and micro-CT study may be inherently linked to the collapse of the c-axis at higher potentials (e.g., >4.2 V versus Li/Li^+), which becomes more substantial as the Ni content is increased (e.g., c-axis collapse is more noticeable for NMC811 compared to NMC111) and is associated with lattice collapse, subsequent oxygen loss, and detrimental particle cracking.[22] Moreover, inter-particle variation of the Mn content has also been linked to crystal disorder and lattice variations with cycling.[4]

Efforts have been made to add dopants that can suppress the lattice collapse.[23] In addition, microstructural properties such as particle size have been tailored to increase the homogeneity of phase distributions.[24] Nonetheless, as observed within this work, achieving uniform (de-)lithiation with minimal hysteresis, thus minimizing localized strain maxima, is highly challenging. As demonstrated here, inter- and intraparticle variations in state-of-charge, and consequently lattice parameters, can be expected. This would likely be accompanied by a distribution of strain whereby non-uniform lattice collapse could exacerbate weakness in locations such as grain boundaries or crystallographic defects.

DISCUSSION

To conclude, a new *in situ* electrochemical pouch cell geometry for a wide range of 2D and 3D X-ray characterization techniques is presented, and we have used this specialized pouch cell design in a proof-of-concept spectroscopic TXM study on an NMC811 electrode at its pristine and electrochemically delithiated states, through which local state-of-charge distribution can be monitored at the subparticle level for the same particle across a range of conditions. This has revealed a definitive relationship between manufacturing defects within particles and variations in charge distribution in regions close to the defect zone after delithiation, where such inhomogeneities do not exist in the pristine state. Furthermore, radiation-induced degradation to the carbon and binder domain is observed after prolonged exposure during tomographic acquisition, emphasizing the need for dose-minimization strategies during image acquisition, especially for *in situ* measurements.

In future work, to characterize transient phenomena, 2D spectroscopic TXM will be carried out on optimized versions of the specialized pouch cell with lower mass loading electrodes, which are needed to isolate stacked particles in the absence of 3D data, and a smaller region of interest to enable *operando* imaging. Furthermore, we posit that by acquiring 2D edge energy maps from various angles and increasing the magnification of the post-mortem micro-CT volume, more particle defects may be correlated with state-of-charge variations while minimizing overall acquisition time and radiation exposure. It is hoped that this can shed some light on how particle defects contribute to failure across the electrode lifetime, and the mechanistic effects that strategies such as single-crystal and coated Ni-rich NMC materials have in mitigating degradation. Longitudinal 3D studies may also be carried out on actual electrodes harvested on cells taken to various cycling conditions to develop a better spatial and temporal understanding of the long-term degradation mechanisms behind these Ni-rich NMC materials.

EXPERIMENTAL PROCEDURES

Resource availability

Lead contact

Further information and request for resources should be directed to and will be fulfilled by the lead contact, Paul Shearing (p.shearing@ucl.ac.uk).

Materials availability

This study did not generate any new materials or reagents.

Data and code availability

All of the data reported in this article will be shared by the lead contact upon request. This article does not report original code.

Laser milling of electrode samples

NMC811[+] (NEI Corporation) Li-ion electrode coatings (90:5:5 wt% of NMC811, conductive carbon, and polyvinylidene difluoride [PVDF]) with an areal capacity of ~1.0 mAh cm^{-2} were secured on a Petri dish with polyimide tape and sealed using a glass lid with Parafilm in an Ar-filled glove box before being fixed to the translation table of a laser micromachining instrument (A Series, Oxford Lasers) containing a 532-nm laser with a spot size of ~40 μm. The laser was programmed to mill a series of lines at a speed of ~2 mm s^{-1}, amounting to a pouch cell electrode consisting of a bare current collector on the top right, the main electrode, and a small tab protrusion at the bottom for imaging. The dimensions of the 3 sections were 20 × 4 mm for the bare current collector tab, 15 × 20 mm for the main electrode, and 0.08 × 0.5 mm for the tab protrusion.

Pouch cell preparation

The laser-cut electrode tabs as described above were dried for 12 h under vacuum at 120°C in a glass drying oven (B-585, BUCHI) before being assembled into pouch cells with laminated Al pouch foil (EQ-alf-100-210, MTI Corporation). A half-cell electrode arrangement was used with the NMC811 tab electrode as the working electrode and 120-μm-thick Li metal (Goodfellow) as the counter and reference electrode. A trilayer polyolefin membrane was used as a separator (Celgard 2325), and the electrolyte used was 1.0 M Li hexafluorophosphate in ethylene carbonate and ethyl methyl carbonate, with 2% by weight of vinylene carbonate additive (1.0 M $LiPF_6$ in EC:EMC (3:7 v/v) + 2% VC, SoulBrain MI).

Electrochemical characterization of tab pouch cell

The mass of the active material on the pouch cell electrode was found to be 17.2 mg with an active area of ~3 cm^2; the tab section for imaging has a negligible contribution to the total area. After imaging the cell at the pristine state, described below, the cell was delithiated using a constant-current-constant-voltage (CC-CV) charge protocol on a low-current potentiostat (SP-200, Bio-Logic SAS), with a constant current step of 0.75 mA (equivalent to a ~C/5 rate, assuming a theoretical specific capacity of 220 mAh g^{-1} at 4.3 V versus Li/Li^+) until an upper cutoff potential of 4.3 V was reached, followed by a constant potential hold at 4.3 V until the current tapered down to C/20, equivalent to ~0.19 mA.

Spectroscopic transmission X-ray microscopy and image processing

Spectroscopic transmission X-ray microscopy was performed at the 6-2c beamline at the Stanford Synchrotron Radiation Lightsource (SSRL). Collected were 15 × 3 mosaics, with 25% overlap between the tiles, encompassing the whole imaging tab section of the specialized pouch cell. The field of view of each tile was ~30 μm, consisting of 1,024 × 1,024 pixels, with a pixel size of 37.4 nm at 8,950 eV. Each mosaic was acquired at 7 energy steps around the Ni k-edge; 8,300 eV and 8,320 eV for the pre-edge region; 8,347.5, 8,353, and 8,360 eV around the edge; and 8,800 and 8,950 eV for the post-edge region. The energy points were chosen to maximize the anticipated contrast between Ni oxidation states while minimizing the radiation dose to

the electrode. The mosaic images were then processed in the TXM-Wizard software suite, with reference correction, magnification correction, image alignment, mosaic stitching, and TXM-XANES analysis, all of which are described elsewhere.[8,20] The edge energy maps saved by TXM-Wizard were exported into 64-bit .raw files using MATLAB and then imported into the Avizo software suite (FEI SAS, France) for visualization.

Micro-CT imaging

X-ray micro-CT was performed on the same pouch cell after the completion of the experiment at SSRL. A lab-based micro-CT instrument (Zeiss Xradia Versa 520, Carl Zeiss) was used, containing a polychromatic microfocus sealed source set to an accelerating voltage of 120 kV on a tungsten target at a maximum power of 10 W. The scintillator was coupled to a 40× objective lens and 2,048 × 2,048-pixel CCD detector with a pixel binning of 2, resulting in a pixel size of 345.5 nm and a field of view of ~350 μm. The sample was rotated through 360° with radiographs collected at discrete angular intervals amounting to a total of 1,201 projections. The radiographic projections were then reconstructed with the OptiRecon software suite (OptiRecon, Carl Zeiss) using a proprietary iterative algorithm for cone beam geometry.

Image processing in Avizo

Image processing was performed in Avizo (V2020.2, Thermo Fisher Scientific) on the reconstructed micro-CT volume containing 975 × 975 × 975 voxels and the edge energy maps extracted from the output of TXM-Wizard described earlier. Segmentation of the NMC particles was carried out via a simple thresholding algorithm derived from Otsu's method[25] and available in the Auto-Threshold module in Avizo. Small features <5 voxels wide were removed, and the Separate Objects Avizo module was applied to separate neighboring particles that were in contact with one another. The separated particles were individually labeled using the Label Analysis Avizo module, which assigns different label values to each particle. A Z projection of the micro-CT grayscale dataset was obtained using the Image Stack Projection module in Avizo, to emulate the TXM mosaics. Another intensity-maxima projection of the individually numbered particle label field was also obtained using the Image Stack Projection module in Avizo to show any stacking of particles in the direction orthogonal to the current collector. All of the datasets were manually aligned using the Transform Editor tool in Avizo.

ACKNOWLEDGMENTS

This work was carried out with funding from The Faraday Institution (https://faraday.ac.uk; EP/S003053/1), grant nos. FIRG001, FIRG024, and FIRG028. The authors would like to acknowledge the Royal Academy of Engineering (CiET1718/59) for financial support. Access to the ZEISS Xradia 810 Ultra instrument was supported by the EPSRC (EP/K005030/1). Access to the 6-2c beamline at the Stanford Synchrotron Radiation Lightsource, SLAC National Accelerator Laboratory, is supported by the US Department of Energy, Office of Science, Office of Basic Energy Sciences, under contract no. DE-AC02-76SF00515.

AUTHOR CONTRIBUTIONS

C.T., A.S.L., and T.M.M.H. performed the experiments with J.N.W. C.T., A.S.L., T.M.M.H., and H.P. performed the data analysis. C.T. wrote the manuscript, with input from all of the authors. R.J., D.J.L.B. and P.R.S. provided supervision of the work.

DECLARATION OF INTERESTS

The authors declare no competing interests.

Received: June 25, 2021
Revised: September 2, 2021
Accepted: October 25, 2021
Published: November 12, 2021

REFERENCES

1. Li, T., Yuan, X.-Z., Zhang, L., Song, D., Shi, K., and Bock, C. (2019). Degradation Mechanisms and Mitigation Strategies of Nickel-Rich NMC-Based Lithium-Ion Batteries. Electrochem. Energy Rev. *3*, 43–80.

2. Skeete, J.-P., Wells, P., Dong, X., Heidrich, O., and Harper, G. (2020). Beyond the EVent horizon: battery waste, recycling, and sustainability in the United Kingdom electric vehicle transition. Energy Res. Soc. Sci. *69*, 101581.

3. Heenan, T.M.M., Tan, C., Hack, J., Brett, D.J.L., and Shearing, P.R. (2019). Developments in X-ray tomography characterization for electrochemical devices. Mater. Today *31*, 69–85.

4. Heenan, T.M.M., Wade, A., Tan, C., Parker, J.E., Matras, D., Leach, A.S., Robinson, J.B., Llewellyn, A., Dimitrijevic, A., Jervis, R., et al. (2020). Identifying the Origins of Microstructural Defects Such as Cracking within Ni-Rich NMC811 Cathode Particles for Lithium-Ion Batteries. Adv. Energy Mater. *10*, 2002655.

5. Nelson Weker, J., and Toney, M.F. (2015). Emerging In Situ and Operando Nanoscale X-Ray Imaging Techniques for Energy Storage Materials. Adv. Funct. Mater. *25*, 1622–1637.

6. Cao, C., Toney, M.F., Sham, T.-K., Harder, R., Shearing, P.R., Xiao, X., and Wang, J. (2020). Emerging X-ray imaging technologies for energy materials. Mater. Today *34*, 132–147.

7. Liu, Y., Meirer, F., Wang, J., Requena, G., Williams, P., Nelson, J., Mehta, A., Andrews, J.C., and Pianetta, P. (2012). 3D elemental sensitive imaging using transmission X-ray microscopy. Anal. Bioanal. Chem. *404*, 1297–1301.

8. Meirer, F., Cabana, J., Liu, Y., Mehta, A., Andrews, J.C., and Pianetta, P. (2011). Three-dimensional imaging of chemical phase transformations at the nanoscale with full-field transmission X-ray microscopy. J. Synchrotron Radiat. *18*, 773–781.

9. Yang, F., Liu, Y., Martha, S.K., Wu, Z., Andrews, J.C., Ice, G.E., Pianetta, P., and Nanda, J. (2014). Nanoscale morphological and chemical changes of high voltage lithium-manganese rich NMC composite cathodes with cycling. Nano Lett. *14*, 4334–4341.

10. Tian, C., Xu, Y., Nordlund, D., Lin, F., Liu, J., Sun, Z., Liu, Y., and Doeff, M. (2018). Charge Heterogeneity and Surface Chemistry in Polycrystalline Cathode Materials. Joule *2*, 464–477.

11. Pattammattel, A., Tappero, R., Ge, M., Chu, Y.S., Huang, X., Gao, Y., and Yan, H. (2020). High-sensitivity nanoscale chemical imaging with hard x-ray nano-XANES. Sci. Adv. *6*, eabb3615.

12. Xu, Z., Jiang, Z., Kuai, C., Xu, R., Qin, C., Zhang, Y., Rahman, M.M., Wei, C., Nordlund, D., Sun, C.J., et al. (2020). Charge distribution guided by grain crystallographic orientations in polycrystalline battery materials. Nat. Commun. *11*, 83.

13. Wang, J., Chen-Wiegart, Y.C., and Wang, J. (2013). In situ chemical mapping of a lithium-ion battery using full-field hard X-ray spectroscopic imaging. Chem. Commun. (Camb.) *49*, 6480–6482.

14. Wang, J., Chen-Wiegart, Y.C., and Wang, J. (2014). In operando tracking phase transformation evolution of lithium iron phosphate with hard X-ray microscopy. Nat. Commun. *5*, 4570.

15. Tan, C., Daemi, S.R., Taiwo, O.O., Heenan, T.M.M., Brett, D.J.L., and Shearing, P.R. (2018). Evolution of Electrochemical Cell Designs for In-Situ and Operando 3D Characterization. Materials (Basel) *11*, E2157.

16. Alvarado, J., Wei, C., Nordlund, D., Kroll, T., Sokaras, D., Tian, Y., Liu, Y., and Doeff, M.M. (2020). Thermal stress-induced charge and structure heterogeneity in emerging cathode materials. Mater. Today *35*, 87–98.

17. Tan, C., Daemi, S., Heenan, T., Iacoviello, F., Leach, A.S., Rasha, L., Jervis, R., Brett, D.J.L., and Shearing, P.R. (2020). Rapid Preparation of Geometrically Optimal Battery Electrode Samples for Nano Scale X-ray Characterisation. J. Electrochem. Soc. *167*, 060512.

18. Nelson, J., Yang, Y., Misra, S., Andrews, J.C., Cui, Y., and Toney, M.F. (2013). Identifying and managing radiation damage during in situ transmission x-ray microscopy of Li-ion batteries. Proc. SPIE *8851*. https://doi.org/10.1117/12.2027263.

19. Lim, C., Kang, H., De Andrade, V., De Carlo, F., and Zhu, L. (2017). Hard X-ray-induced damage on carbon-binder matrix for in situ synchrotron transmission X-ray microscopy tomography of Li-ion batteries. J. Synchrotron Radiat. *24*, 695–698.

20. Liu, Y., Meirer, F., Williams, P.A., Wang, J., Andrews, J.C., and Pianetta, P. (2012). TXM-Wizard: a program for advanced data collection and evaluation in full-field transmission X-ray microscopy. J. Synchrotron Radiat. *19*, 281–287.

21. O'Grady, W.E., Pandya, K.I., Swider, K.E., and Corrigan, D.A. (1996). In situ x-ray absorption near-edge structure evidence for quadrivalent nickel in nickel battery electrodes. J. Electrochem. Soc. *143*, 1613–1616.

22. Ryu, H.-H., Park, K.-J., Yoon, C.S., and Sun, Y.-K. (2018). Capacity Fading of Ni-Rich Li [NixCoyMn1–x–y]O2 ($0.6 \leq x \leq 0.95$) Cathodes for High-Energy-Density Lithium-Ion Batteries: Bulk or Surface Degradation? Chem. Mater. *30*, 1155–1163.

23. Yang, J., and Xia, Y. (2016). Suppressing the Phase Transition of the Layered Ni-Rich Oxide Cathode during High-Voltage Cycling by Introducing Low-Content Li2MnO3. ACS Appl. Mater. Interfaces *8*, 1297–1308.

24. Li, J., Shunmugasundaram, R., Doig, R., and Dahn, J.R. (2015). In Situ X-ray Diffraction Study of Layered Li–Ni–Mn–Co Oxides: Effect of Particle Size and Structural Stability of Core–Shell Materials. Chem. Mater. *28*, 162–171.

25. Otsu, N. (1979). A Threshold Selection Method from Gray-Level Histograms. IEEE Trans. Syst. Man Cybern. *9*, 62–66.